Lipid mapping in human dystrophic muscle by cluster-time-of-flight secondary ion mass spectrometry imaging.

Nora Tahallah, Alain Brunelle, Sabine de La Porte, Olivier Laprévote

Published in final edited form as:
J. Lipid Res. 2008.49: 438-454.

Lipid mapping in human dystrophic muscle by cluster-time-of-flight secondary ion mass spectrometry imaging

Nora Tahallah[1], Alain Brunelle[1], Sabine De La Porte[2], Olivier Laprévote[1]

[1] Laboratoire de Spectrométrie de Masse, Institut de Chimie des Substances Naturelles, CNRS, UPR 2301, Av. de la Terrasse, F91198, Gif sur Yvette Cedex, France

[2] Laboratoire de Neurobiologie Cellulaire et Moléculaire, Institut de Neurobiologie Alfred Fessard, CNRS, FRC2118, UPR 9040, Av. De la Terrasse, F91198, Gif sur Yvette Cedex, France

Correspondence should be addressed to:

Olivier Laprévote

Laboratoire de Spectrométrie de Masse, Institut de Chimie des Substances Naturelles

CNRS, Avenue de la Terrasse, F-91198 Gif sur Yvette Cedex

Phone: 33 (0)1 69 82 30 32

Fax: 33 (0)1 69 07 72 47

email: Olivier.Laprevote@icsn.cnrs-gif.fr

Abstract

Human striated muscle samples, from male control and Duchenne Muscular Dystrophy (DMD)-affected children, have been subjected to cluster-time-of-flight secondary ion mass spectrometry (cluster-ToF-SIMS) imaging, using a 25 keV Bi_3^+ liquid metal ion gun, under static SIMS conditions. Spectra and ion density maps, or secondary ion images, have been acquired in both positive and negative ion mode over several areas of 500 x 500 μm^2 (image resolution 256 x 256 pixels). Characteristic distributions of various lipids have been observed. Vitamin E and phosphatidylinositols have been found to concentrate within the cells, whereas intact phosphocholines accumulated over the most damaged areas of the dystrophic muscles, together with cholesterol and sphingomyelin species. Fatty acyl chains composition varied depending on the region, allowing estimation of the local damage extent.

Supplementary keywords: Duchenne Muscular Dystrophy; Human Skeletal Muscle Degeneration; Lipidomics; Mass Spectrometry Imaging; ToF-SIMS; Oxidative Stress; Regeneration.

Introduction

First described by the French doctor Duchenne de Boulogne in the XIXth century, Duchenne muscular dystrophy (DMD) is a severe degenerative genetic disease. Almost exclusively male children develop this myopathy, with an estimation of 1 in 3 500 boys worldwide (1). This X-linked recessive pathology is induced by absence of expression or by truncation of dystrophin, a 427 kDa cytoskeletal protein involved in a transmembrane noncovalent complex of more than 20 proteins. The lack of dystrophin causes a rapid progression of skeletal, smooth and cardiac muscles degeneration. Result then, already from the age of 2 or 3, bad posture, unsteady gait, difficulty in standing, walking or climbing stairs. A rolling chair is necessary around 10 to 12 years old and patients inexorably die around the age of 25-30. Dystrophin deficiency hampers the formation of an essential transmembrane complex in charge of the integrity of muscle cell walls. This results in muscle cell membranes malfunctioning and permeability, alteration of the ion drifts through the membrane (*e.g.* calcium), but also in oxidation stress. Diagnoses are mainly based on analyses of creatin kinase level in the serum and electromyograms associated to biopsies or genetic tests. Among the therapies used to decelerate the damages caused by the disease, are found dystrophin-associated drug design, gene and cell therapies or utrophin-associated therapies (2). Up to date, there is unfortunately no cure for DMD yet.

This last decade, research has been going on using different animal models (mice, dogs, cats, drosophila and *Caenorabditis* worms) to get a better understanding of this lethal pathology mechanisms. The dog model, closest to human, is rare and expensive and, although cheaper and more accessible, drosophila and *Caenorabditis* worms phenotypes are too different from the human one. The most spread model is the *mdx* (X-linked muscular dystrophy) mouse, developing an unusually high concentration of creatin and pyruvate kinases (3). The three

advantages of the *mdx* mouse model are relatively low cost, good availability and relatively short lifetime.

To gain more insight on Duchenne muscular dystrophy, our group has previously carried out investigations on an *mdx* mouse leg muscle. Matrix-Assisted Laser Desorption Ionization-Time-Of-Flight (MALDI-TOF) profiling (4) and cluster-Time-of-Flight Secondary Ion Mass Spectrometry (cluster-ToF-SIMS) imaging (5) have been performed on 3 weeks old *mdx* mice, as well as on control (*nxlt*) and dystrophic (*xlt*) mice myoblast cell cultures. These studies allowed distinguishing three regions in the *mdx* mouse leg: a severely damaged region, a second one degenerating and undergoing oxidative stress and phosphatidylinositol cycle deregulation and a third one that was found stable.

Concerning ToF-SIMS, its input is continuously expanding in the field of lipidomics and drugs/biomarkers mapping on biological tissues at a micrometer scale (6). ToF-SIMS imaging has the major advantage, over alternative methods, of allowing direct and simultaneous collection of mass spectra and ion images. Retrieval of molecular composition and individual compound localization on a tissue section, at micrometer scale and without the need of any prior sample treatment, makes then the analyses easier, more straightforward and the closest possible to the physiological conditions. Recent innovations, such as Bismuth (Bi_3^+) primary ion cluster sources (7), have tremendously enhanced the secondary ion emission yield of larger secondary ions. This development extended the capabilities of the method, rendering this approach particularly attractive and suitable for the investigation of biological tissues (8,9,10,11,12,13,14,15,16).

In order to validate the coupling of the ToF-SIMS imaging methodology, together with the *mdx* mouse model, as a suitable approach for research on the human pathology, we here report on first results obtained on human striated muscle sections and compare them to the previous outcomes on the *mdx* mouse. Therefore cluster-ToF-SIMS imaging has been used to map and

characterize the molecular distribution in human control and dystrophic muscle tissue sections. Mass spectra revealed differences in the distribution of fatty acids, phospholipids, di- and triglycerides. Samples were analyzed in both positive and negative ion modes. The negative ion mode spectra displayed signals in the region *m/z* 200-350, corresponding to the palmitic (C16:0, *m/z* 255.2), palmitoleic (C16:1, *m/z* 253.2), stearic (C18:0, *m/z* 283.2), oleic (C18:1, *m/z* 281.2), linoleic (C18:2, *m/z* 279.2) and arachidonic (C20:4, *m/z* 303.2) fatty acid carboxylate (FA) ions. Between *m/z* 350 and 450, signals originated from cholesterol and α-tocopherol (vitamin E). Phospholipids and triglycerides were found between *m/z* 600 and *m/z* 900. The DMD-affected muscles displayed different distribution of these ions in the dystrophic cells and in the severely damaged areas. Positive ion mode spectra confirmed the variation in intensity of cholesterol and vitamin E in the different areas. The proportion of phosphatidylcholines also varied with the extent of degradation of the tissue. The ion images allowed differentiating the regions where accumulation of these different compounds occurred either in dystrophic cells, severely damaged areas or adipocytes.

Materials and Methods

Surgery residues of human paravertebral striated muscles, from male control and DMD-affected 12 to 14 years old children were provided by the *"Banque de Tissus pour la Recherche"* (BTR, Institut de Myologie Hôpital de la Pitié-Salpêtrière, 83 boulevard de l Hôpital, 75013 Paris) after approval of the project.

Histological staining

10 µm thick sections were cut at -20°C in a CM3050-S cryostat (Leica Mycrosystèmes SA, Rueil-Malmaison, France) and immediately deposited onto a glass plate then stored at -80°C for histological staining. The dystrophic appearance of the human paravertebral striated muscle was studied with Masson's trichrome staining (Sigma kit No. HT15) to visualize

muscle fibers (in red), connective tissue and collagen (colored by the aniline blue). Histological images were taken with a DMRXA2 microscope (Leica Mycrosystèmes SA, Rueil-Malmaison, France).

Sample preparation for cluster-ToF-SIMS Imaging

Cryostat sections (20 µm) were prepared, placed on glass plates and briefly stored at -80°C. Immediately before analyses, samples were dried under a few millibars pressure for 30 minutes, without any further treatment. Then, images were recorded with an Olympus BX51 microscope (Rungis, France) equipped with 1.25x to 50x lenses and a Color View I camera (Soft Imaging System) monitored by the Olympus DP Soft software.

ToF-SIMS data acquisition and processing

All experiments were performed on a commercial ToF-SIMS IV (ION-TOF GmbH, Münster, Germany) reflectron-ToF mass spectrometer located at the French "*Institut de Chimie des Substances Naturelles*" in Gif-sur-Yvette, France. The instrument was fitted with a bismuth (Bi_3^+) cluster ion source at a 45° incidence angle. The primary ion dose density was 2 x 10^{11} ions/cm^2 for each ion mode, with a 150 µs cycle time and a 0.27 pA measured pulsed current. The ion column focusing mode ensured both a 1-2 µm beam focus and a high mass resolution, which is a prerequisite for accurate mass measurements and assignments. A low-energy electron flood gun neutralized the surface during analysis. The secondary ions were first extracted with a 2 keV kinetic energy, had an effective ion flight path of ~2m and were then post-accelerated to 10 keV before hitting the detector surface. The sample surface was directly observable through an integrated video camera. Positive and negative secondary ion images, obtained with IonImage software, had a field of view of 500 x 500 μm^2 (256 x 256 pixels). Images were compressed during data processing to 128 x 128 pixels to increase the contrast, leading to a final lateral resolution of 4 µm. For more clarity, images were also averaged and rescaled. To ensure the correct localization on each spot, a thorough

examination was performed for each compound: an image was generated for each peak of the isotopic distribution of the compound (*i.e.* for the ^{12}C atoms containing peak, for the $^{13}C_1$ containing peak and for the peak containing two ^{13}C). These images were then matched and summed to obtain the final compound image. However, in cases like PC34:2 (see section isotopic correction for details), only the first two images were summed. Subsequently, Regions Of Interest (ROIs) were manually selected and the corresponding mass spectra were extracted to obtain local information. These selected regions may have different areas. Therefore, and for a proper comparison, the spectrum corresponding to each ROI needed to be normalized against the area of the smallest one. In the following, the selected cells, intercellular and damaged areas are characteristic of all the different types of cells, intercellular and damaged areas contained in the analyzed sections.

Calibration and mass assignments

The method was the same as in reference (5). The very low initial secondary ions kinetic energy (17) allows a linear relationship between the time of flight and the square root of *m/z* over the whole mass range. Therefore, an internal calibration is possible, using the signals of H^+, H_2^+, H_3^+, C^+, CH^+, CH_2^+, CH_3^+, trimethylammonium ($C_3H_{10}N^+$, *m/z* 60.08), a choline fragment ($C_5H_{12}N^+$, *m/z* 86.10), choline ($C_5H_{14}NO^+$, *m/z* 104.10) and phosphatidylcholine ($C_5H_{15}O_4NP^+$, *m/z* 184.07) for the positive ion mode and the signals of C^-, CH^-, CH_2^-, C_2^-, C_3^-, C_4H^-, PO_2^- (*m/z* 62.96), PO_3^- (*m/z* 78.96), $H_2PO_4^-$ (*m/z* 96.97) for the negative ion mode. Signals of the fatty acid carboxylate ions and vitamin E deprotonated molecule were used for the negative ion mode calibration refinement. For the positive ion mode, cholesterol fragment and deprotonated molecule, deprotonated vitamin E and diglyceride fragment signals were selected. Due to the lack of an efficient MS-MS method which could be associated to TOF-SIMS imaging, structure attributions or assignments of ion peaks were made according to the instrument resolution and accuracy, the valence rule, the biological characteristics of the

tissue, as already mentioned in details in reference (5). Many mass assignments have also been confirmed or at least reinforced with the help of the literature. Details will be given as one goes along in the next sections.

Calculation of lipid intensity ratios with isotopic correction

In this report, the intensity refers to the area of the ion peak in the corresponding mass spectrum. Large mass lipids, *e.g.* phosphatidylcholines (PCs), contain an important number of carbons. Therefore, the positive ion mode PC34:2 signal is composed of 60.7 % monoisotopic peak (*m/z* 758.6), 29.5 % of $^{13}C_1$ containing ions (*m/z* 759.6) and 8 % with two ^{13}C (*m/z* 760.6). This latter peak contributes thus to the intensity of the PC34:1 monoisotopic peak at *m/z* 760.6. Besides, the emission yields and detection efficiencies for compounds of the same family and close molecular weight are considered equivalent (18). Hence, when calculating phosphatidylcholines intensity ratios the isotopic contribution correction has been applied. For the sake of precision, the calculation of the fatty acids intensity ratios, in negative ion mode, was also performed taking into account this same correction.

Ratios definition

$R_1 = I_{m/z\ 758} / I_{m/z\ 760}$. R_1 is the ratio of the intensity of the PC34:2 protonated molecule signal at *m/z* 758.6 over the corrected intensity of the PC34:1 protonated molecule signal at *m/z* 760.6, in the positive ion mode. $R_2 = I_{m/z\ 283} / I_{m/z\ 281}$. R_2 is the ratio of the corrected intensity of the C18:0 fatty acid carboxylate signal at *m/z* 283.2 over the intensity of the C18:1 fatty acid carboxylate signal at *m/z* 281.2, in the negative ion mode. $R_3 = I_{m/z\ 281} / I_{m/z\ 279}$. R_3 is the ratio of the corrected intensity of the C18:1 fatty acid carboxylate signal at *m/z* 281.2 over the intensity of the C18:2 fatty acid carboxylate signal at *m/z* 279.2, in the negative ion mode.

Results

We investigated human striated muscle originating from surgery residues of one control (12 years old) and two distinct DMD-affected (13 and 14 years old) children. Four cryosections from the control and two sections from each DMD-affected muscle were selected. On each section, 2 to 6 zones were subjected to ToF-SIMS imaging. These 33 ToF-SIMS analyzed zones (13 control and 20 dystrophic) will be referred to as spots, in the following, for more clarity.

Fig. 1A shows the microscope optical image of a section from a control 12 years old child surgery residue. In green is delimited spot 1, one of the areas subjected to ToF-SIMS analyses. Individual, compact and regular myofibers (muscle cells) are visible, all sheathed by a membrane in whole fascicles. Fig. 1B displays the microscope optical image of a section from a 14 years old DMD-affected child surgery residue and in green are highlighted two of the analyzed spots (2 and 3) described in this report. Physical differences are visible between nonstructured, damaged and pseudo-healthy zones. The colors vary and fibers membrane sheaths are absent. Although the myofibers are clearly observed, they are not regularly sized and only few zones appear more compact. Finally, these two images helped us to choose the areas to be analysed by mass spectrometry imaging on the DMD-affected muscle sections.

Histology of control and DMD-affected human striated muscle sections

As a start, to probe the physiological status of the muscles and visualize connective tissue, muscle fibers and collagen, we applied to control and dystrophic human striated muscle sections a Masson's trichrome staining. The healthy muscle fibers in Fig. 2A appear (in red) regular, compact within a fascicle membrane surrounded by only a minute amount of collagen (in blue). Conversely, the DMD-affected muscle cells (Fig. 2B) are irregular, dislocated, lacking fascicle membrane and surrounded by an important amount of collagen and connective tissue within the numerous damaged areas.

ToF-SIMS spectrum from a control muscle section

A control human striated muscle has first been analyzed by ToF-SIMS imaging (*e.g.* spot 1, Fig. 1A). The total mass spectrum of spot 1 recorded in positive ion mode is displayed in Fig. 3 (mass range *m/z* [80-820]). Choline and phosphatidylcholine fragment ions at *m/z* 86.1, 104.1, 125.0, 184.1 have already been identified by many authors and their structure are given in reference (4), while the phosphatidylcholine fragment ion at *m/z* 224.1 has been identified by TOF-SIMS Post Source Decay measurements directly onto a rat brain section (19). The cholesterol ions, at *m/z* 369 and *m/z* 385, in positive ion mode have been already mentioned in many papers such as (10), (11) and (20). Positive ions of vitamin E have been identified in previous imaging experiments (5,12). Series of positive ions are observed in the *m/z* 500-620 range. These ions are likely to be fragments of diglycerides (DGs), triglycerides (TGs), PCs, or phosphatidylinositols (PIs). These ions are labeled with a generic name "DG type fragment". Their ion images (data not shown) reveal a general colocalization with triglycerides, suggesting that these "DG type fragment" ions mainly originate from fragmentation of diglycerides and triglycerides. PC positive ions in the region *m/z* 750-810 have already been observed and characterized in ToF-SIMS imaging experiments by several authors (5,10,11). In particular, the structure of these ions has already been studied directly from mouse muscular cell cultures by MALDI-TOF tandem mass spectrometry (4). Finally the ion detected at *m/z* 723.5 might tentatively be attributed to a sodiated sphingomyelin (SM) ion.

As the mouse samples, the human muscle sections also exhibit intact PC ions as the dominant species in the region *m/z* [650-820], principally PC34:2 and PC34:1 (*m/z* 758.6 and 760.6, respectively) and their respective sodium adducts at *m/z* 780.6 and 782.6 and potassium adducts at *m/z* 796.6 and 798.6. It must be mentioned that PC34:2 and PC34:1 ions are not the only PCs ions which are detected. Several other PC ion species appear are also present in the

spectra, as it was the case for the previous studies on model mice (4,5). PC fragments appear in the region *m/z* [80-300].

ToF-SIMS imaging of phosphatidylcholines

Fig. 4A depicts, from left to right, the microscope image of spot 1, the images of the *m/z* 758 and 760 ions over the analyzed surface as well as the selected ROIs. Indeed, ToF-SIMS imaging gives the opportunity to select particular regions of interest (ROIs) on the analyzed surface and to extract, from each of them, the corresponding spectrum. Therefore, to obtain a more precise information, we have selected different ROIs within spot 1 (Fig. 4A, right), driven by the different distributions on the ion images. In red, green and blue are selected cells and in pink an intercellular space. From each ROI a mass spectrum was extracted, as shown in Fig. 4B, and the corresponding PC34:2/PC34:1 (758.6/760.6) intensity ratio was calculated. For the sake of clarity, this ratio is referred to as R_1 in the following. Most of the selected regions led to a R_1 ratio value of around 2 (Fig. 4C). By contrast, a unique cell (selected in green) gave R_1 at 0.80. The ion images (Fig. 4A) pointed as well to this cell as the only area where the *m/z* 758 ion intensity is clearly lower than the 760's. If the present results are to be compared with those obtained from the *mdx* mouse model (4), this means that this might well be a regenerating cell.

We have then analyzed the different DMD-affected muscle sections and the results are illustrated by two typical examples in Figs. 5 and 6. A first pseudo-healthy region, containing almost exclusively highly uniform and compact cells, drew our attention (Fig. 5). We focused on this spot (numbered 2 in Fig. 1B) to start the comparison between the control and the DMD-affected samples. The value of ratio R_1, for the whole spot 2, was 1.27 (see Table I: DMD section 1), in accordance again with the *mdx* mouse model. However, the mass spectra (Fig. 5B) corresponding to the selected ROIs (Fig. 5A, right), and the R_1 values of the different ROIs reported in Fig. 5C showed that the cells were not fully identical, in terms of

PCs composition, over this zone. Indeed, the small cells (blue ROI) exhibited a R_1 ratio value of 1.26. However, the larger cells split in two: some cells (in red) generated a ratio value of 1.21, similarly to the small ones, while others (in green) gave an R_1 ratio value of 1.42. The large cells delimited by the green ROI then presented a PCs composition similar to that of the healthy tissue, whereas the intercellular space (R_1=0.71) behaved like a regeneration zone. The big cells in the red ROI and the small cells in the blue ROI appeared to be in an intermediate state.

The second characteristic region of the DMD-affected human muscle is typified by spot 3 (Fig. 1B). The R_1 global ratio value for this spot was determined to be 1.13 (Table I: DMD section 1), suggesting an *m/z* 758.6 ion slightly more abundant than the *m/z* 760.6 ion. Fig. 6A depicts, from left to right, the microscope image, the images of the ions at *m/z* 758 and 760 and the selected ROIs over spot 3. For more detailed information, we chose ROIs corresponding to three morphologically different regions (Fig. 6A, right): relatively ordered cells were selected in red, a damaged area in green and some adipocytes in blue. Fig. 6B shows the mass spectra of each of these selected ROIs (*m/z* [650-820]), while Fig. 6C displays the corresponding R_1 values (1.04 within the cells and 0.83 in the damaged region). In the mass spectrum of the blue ROI (adipocytes), the signal-to-noise ratio was not sufficient to determine the R_1 ratio. Thus, in the DMD spot 3, the relatively ordered cells exhibit a similar behavior to that of the control zones in the *mdx* mouse model. On the other hand, the damaged area generated a R_1 value of 0.83, corresponding to that of the intercellular region of the DMD spot 2 and to the green cell of the control spot 1. Similarly to the destructured (regenerating) zone in the *mdx* mouse model, these ratio values were lower than 1.This could denote an intensive regenerating activity and not degeneration, as could be expected from the color, aspect and absence of fascicles on the microscope image of spot 3. Besides, when compared to spot 2, the lower R_1 ratio produced by the cells of spot 3 indicates also that these

cell PCs have incorporated less C18:2, as observed previously in DMD-affected human muscles (21,22). This also means that spot 2 is in a more stable state than spot 3 and confirms the pseudo-healthy nature of spot 2.

The reproducibility of these results was verified on different sections of the same (control and dystrophic) surgery residues and their reliability was validated on sections of a second dystrophin deficient child surgery residue. Table I summarizes the global R_1 ratio calculations performed on all control and dystrophic muscle sections. The control samples provided an average ratio value of 1.85 (with a ± 0.31 standard deviation), higher than the one found for the healthy and control areas of the mouse model (4). For the dystrophic samples, the R_1 average value was calculated to be 1.15 (standard deviation ± 0.17), rather comparable to that found for healthy and control areas of *mdx* mouse. The data shown here matches the results of intensity ratios between m/z 758.6 and 760.6 for healthy and dystrophic cells on day 1 of culture (myoblastes) in Reference 4.

ToF-SIMS imaging of cholesterol and sphingomyelin

A remarkable feature in the *m/z* [650-820] region, is the presence of three signals that we tentatively attributed to the sphingomyelin species, SM34:1 (d18:1/16:0) and SM34:2 (d18:1/16:1 or d18:2/16:0). The mass spectrum of a DMD sample (Fig. 7A, lower spectrum) showed indeed peaks corresponding to the protonated molecule (*m/z* 703.5, $[SM34:1+H]^+$), to the sodium adduct (*m/z* 725.5, $[SM34:1+Na]^+$) and to a fragment possibly corresponding to the choline headgroup elimination from the sodiated lipid (*m/z* 668.4). These ions have been previously described in the literature for membrane sphingolipids (23), which have been reported to be involved in the activation of ion channels and functional rafts (24,25) and to be colocalized with them (26). Sphingomyelins are now known to colocalize with cholesterol and form rafts in plasma membranes of cultured cells (27,28) and PCs and cholesterol have been found to interact in membrane bilayers (28,29). The ion images of spot 3 revealed indeed

a maximum of cholesterol species (Fig. 8A) and SMs species in the damaged region together with PC34:2 and PC34:1 (Fig. 8B). For the pseudo-healthy spot 2, a maximal accumulation of SM and cholesterol species was found in the intercellular region. The other analyzed spots confirmed their colocalization in intercellular or damaged areas. It is noteworthy that, in spot 2, some SM species were also present in the small cells unlike in the large ones. For the control spot 1, practically no sphingomyelin ion was detected except the *m/z* 723.5 species, tentatively assigned to the sodiated SM34:2, that gave some signal all over the spot surface (data not shown), together with ions at *m/z* 758.6 and 760.6. In this sample, cholesterol only accumulated in intercellular spaces or adipocytes but not in cells.

ToF-SIMS spectra of fatty acids

The mass spectra recorded in the negative ion mode (enlargement *m/z* [240-320]) of control and dystrophic muscles are displayed in Fig. 7B. Distributions appear distant of 28 mass units (u) with peaks separated by 2 u, characteristic of fatty acid carboxylate ions with different chain lengths bearing a variable number of double bonds (5). In control and DMD-affected samples the same series of fatty acid ions were present. However, their intensities varied according to the nature of the sample.

Table II summarizes the global fatty acid abundance ratios R_2 (C18:0/C18:1) for each analyzed spot of the control and dystrophic muscles, calculated as described in the Materials and Methods section. The control sample spots exhibited an average ratio (0.77 ± 0.16) about 1.5 times higher than the dystrophic ones (0.54 ± 0.14). These values significantly depended on the relative abundance of the cells in the spot area. A more thorough examination of the different ROIs ratios within each DMD-affected spot showed that the cells presented R_2 values of 0.6-0.9, *i.e.* higher than the average value. In other words, for the DMD-affected sections, the higher global ratios (~0.7) corresponded to pseudo-healthy regions and to spots containing healthier cells. The lower ratios were obtained from the most damaged spots

(~0.3). The DMD intercellular or damaged regions gave R_2 values of 0.4-0.5, versus ~0.8 for the control intercellular regions. The adipocytes in the dystrophic spot 3 exhibited a ~0.4 R_2 value as well.

An additional striking feature is the generally high level of C18:2 in the control human muscle (Fig. 7B). In Table III, an average value of 0.98 ± 0.18 has been calculated for the R_3 (C18:1/C18:2) ratios in the control samples, while it reached 1.96 ± 0.44 for the dystrophic muscles. Hence, this ratio might also be an indicator of the DMD disease, since the control average R_3 is twice smaller than the dystrophic one. Moreover, the most structured spots in the DMD tissue sections also exhibited a relatively low C18:1/C18:2 ratio value (1.09 and 1.20, spots 1 of DMD sections 3 and 4, respectively), corroborating the healthier state of the cells in these areas.

ToF-SIMS imaging of phosphatidylinositols and triglycerides

In the negative ion mode, Touboul *et al.* (5) localized PIs fragments, at *m/z* 223.0 and 241.0, together with TGs and fatty acid carboxylate ions, in the degenerating area of the *mdx* mouse muscle sections. Their observation suggested that the fatty acid carboxylate ions could originate not only from free fatty acids, but also from TGs fragmentations, as previously observed by ESI-MS (30,31), CF-LSIMS (32) and FAB-MS (33).

For the human samples, the PI fragment ions were present in all mass spectra, together with ions at *m/z* 259.0 and 299.0 (two other PI characteristic fragments) (34), and with the C20:4 ion at *m/z* 303.2 (Fig. 7B). The individual mass spectra of ROIs revealed a maximal abundance of these ions within the cells, pointing out the presence of PIs, in particular PI38:4 (*m/z* 885.6) which contains a C20:4 fatty acyl chain (11,35). Phosphatidylinositols and triglycerides ions are observed together in the mass spectrum region *m/z* [760-920] (Fig. 7C), with characteristic series differing by 28 *u* (two methylene groups) and/or 2 *u* (one double bond). Their assignments are based first on the fact that TG ions are only detected in adipose

or DMD-damaged tissues, secondly on the localization similitude between PI38:4 on the one hand, and PI34:0, PI36:2, PI36:1 and the PI fragments, on the other hand. Finally the mass calculation can differentiate a PI ion from a TG one, since the decimal part of a PI ion mass must be beteween".5" and ".6", while the decimal part of a TG ion is between ".7" or ".8". Therefore the ions at *m/z* 831.8 and 857.8 can only be TG50:1 and TG52:2, respectively. The ion at *m/z* 797.7 remains as far as we know unidentified. The relative intensities of these ions varied and, in general, the more the cells were structured, the less the triglycerides were present, in favor of the PIs. To obtain more details, we have examined different ROIs to be able to distinguish the different corresponding distributions. As an example, Fig. 9A displays the mass spectra obtained in the negative ion mode of the three ROIs selected in spot 3 (cells in red, damaged area in green and adipocytes in blue). These spectra were spectacularly different. The images of the major ion peaks (Fig. 9B) led us to distinguish, on a molecular basis, the three regions of interest. The mass spectrum of the blue ROI showed the characteristic signals of triglyceride ions (*m/z* 803.8, 805.8, 827.8, 829.8, 831.8, 833.8, 853.8, 855.8, 857.8, 859.8, 881.8 and 883.8), confirming the lipid storing function of the adipocytes. Additionally, the presence of some of these species in the damaged area intimates that myofibers develop into adipocytes, accordingly to what has been previously observed in the degenerating areas of the *mdx* mouse model and in human dystrophic muscle tissue (36). By contrast, the peaks at *m/z* 835.6, 837.6 and 863.6 (Fig. 9A, red spectrum) can only originate from the phosphatidylinositols PI34:1, PI34:0 and PI36:1, respectively, but not from TGs. The colocalization of the peak at *m/z* 885.5 with these latter ions led us to assign this ion peak to the PI38:4 species and not the TG54:2 molecule, and the peak at *m/z* 861.6 to PI36:2 and not to TG52:0. All images corresponding to these PI38:4 and PI36:2 ions were perfectly superimposed with the localization of the cells (red ROI). Finally, three ion peaks at *m/z* 795.7, 797.7 and 799.7 were detected selectively in the damaged surface. Their absence in the

adipocytes and in the cells suggested that they did stem neither from triglycerides nor from PIs.

Discussion

Dystrophin deficiency generates malfunctioning in the muscle cell membranes, as the transmembrane complex is largely destabilized, deregulating functional ion channels and oxidation reaction cycles (1). Consequently, the absence of dystrophin and of its interactions with the membrane lipids induces membrane degeneration and muscle apoptosis or necrosis. Cell membrane dysfunctioning results in modifications of membrane lipid unsaturations as a consequence of disturbances in the fatty acids metabolism (22). Since phospholipids are key components of muscle cell walls, the characterization of the degeneration/regeneration process, through the characterization of phospholipid composition and localization, becomes essential.

Glycerophosphatidylcholines (PCs) are known to be a major component of muscle cell membrane phospholipids. These lipids bear a quaternary ammonium moiety granting a fixed positive charge which leads to higher signals than the other lipids present in the tissue, thereby facilitating their detection by mass spectrometry. MALDI-TOF profiling on the *mdx* mouse model has shown, in positive ion mode, the presence of PCs as most abundant species in the region *m/z* 700-850, in particular PC34:2 and PC34:1 at *m/z* 758.6 and 760.6, respectively (4). In this lipid nomenclature (37), 34 represents the total number of carbons contained in the fatty acyl chains, with a total of 2 and 1 unsaturations, respectively. Under MALDI conditions, the intensity ratio of the ions at *m/z* 758.6 over 760.6 was found to be bigger than 1 in the pseudo-healthy area of the *mdx* mouse muscle and smaller than 1 in its destructured area. Healthy and dystrophic *mdx* mouse cultured cells exhibited a ratio value greater than 1 at the stage of myoblasts and smaller than 1 after cell fusion in myotubes. This suggested that the destructured areas in the *mdx* muscle were actually undergoing a

regeneration process rather than degeneration. Likewise, ToF-SIMS spectra on *mdx* mouse leg tissue sections also revealed PCs as most abundant species in the region *m/z* 700-850 (5). However, the poor contrast of the ToF-SIMS images of intact PCs did not provide spatial information, thus the composition modification revealed by MALDI-TOF could not be confirmed. Earlier studies (21,22) have also shown that membrane PCs of the human dystrophic muscle incorporated less C18:2 fatty acyl chains than the healthy one, but more C18:1 and C18:0.

Although the experiments have been performed with different samples and methods, *i.e.* mouse by MALDI-TOF and human by ToF-SIMS, the analyses can be qualitatively compared. Indeed, the control samples exhibited generally a R_1 ratio almost twice bigger than the DMD-affected samples and the regenerating areas generated lower ratios. Thus, these ratios followed the same trends as in the *mdx* mouse model, where ratio values were bigger than 1 for the control zones but smaller than 1 for the destructured (regenerating) areas. As an example, Fig. 8 depicts the images of selected ions and their accumulation over spot 3. These images reveal that, in the DMD-affected muscle, the typical PCs fragments colocalize with the parent species PC34:2 and PC34:1 (Fig. 8B) concentrated mainly in the dystrophic damaged region, as mentioned above. The specific localization and the absence of these phosphocholine species in the adipocytes and between the cells, where the low PC concentration is known, confirmed that our sample treatment did not induce any significant molecular delocalization.

Phosphatidylcholines, Cholesterol and Sphingomyelin colocalization

Cholesterol is a versatile essential membrane component involved in steroid hormones production and cell signaling (38), membrane structure and function (39) and synapse formation (40). PC fragments and cholesterol have been found to have a complementary distribution in the rat cerebellum (26) and in capillary blood leukocytes (41). Cholesteryl

sulfate ions have been identified in TOF-SIMS imaging of human skin and renal human samples from a patient suffering from a genetic disease (42). In line, the results obtained by ToF-SIMS imaging of the human control sample showed a complementary distribution of cholesterol, found in intercellular or adipocytes regions (data not shown), and PCs, mainly found within the cells. In contrast, cholesterol, cholesteryl sulfate (Fig. 8A) and intact PCs (Fig. 8B) colocalized in the damaged or intercellular regions of the DMD-affected samples. This has not been explicitly observed with the mouse samples. Hence, the colocalization might originate from a perturbation of the lipid regulation mechanisms, directly or indirectly inducing, in the human dystrophic muscle, a modification of the PCs accumulation.

The three sphingomyelin ion peaks presented in Fig. 7A appeared in all positive ion mass spectra of the DMD-affected samples, while they were quasi absent in the mass spectra of healthy samples. Negative ion mass spectra showed that both control and DMD-affected muscles contained specific SM34:1 fragment ions (data not shown). However, it was substantially more abundant in the dystrophic samples, and increased with the extent of the damage, than in the control ones. These observations suggest that DMD-affected cells might develop a high sphingomyelinase activity induced by a disorder in the regulation of membrane sphingolipid composition. In healthy cells, after stress or apoptotic stimuli, sphingomyelinase is activated. This diminishes the level of sphingomyelin converted into ceramide (a signaling molecule involved in cell differentiation, proliferation and apoptosis) and the dysfunctioning of ceramide-mediated apoptosis pathway induces high levels of sphingomyelin (43). Ceramides (SM derivatives) are vital signaling substances for tumors, forming SM-rich vesicles, and responsible for their proliferation and survival (44). Besides, it has been previously shown that phospholipase C activity increases in dystrophic mouse muscle together with an increase of sphingomyelin and triglycerides (21,45,46). This enzyme converts phosphatidylcholine species into diglycerides and phosphocholine, both precursors

of sphingomyelin and triglyceride biosynthesis (47,48). In line with this hypothesis, in the human dystrophic muscle, the observed increase of sphingomyelin species, in negative ion mode, goes along with a decrease of phosphatidylcholines species, in favor of diglycerides type fragments (emerging from di- and/or triglycerides), in positive ion mode (data not shown). The above cited sphingomyelin species have been observed in cryopreserved human spermatozoa (49) and Low and High Density Lipoprotein (50). Wiseman *et al.* (23) have found higher levels of SM in cancerous human-liver adenocarcinoma than in non-tumorous tissue.

Cholesterol and SMs colocalization in the dystrophic muscle are in agreement with the literature reports on human samples (27) and support our peak assignments. Yet, this is at odds with the *mdx* mouse data where cholesterol mainly accumulated in the degenerating region together with vitamin E. Additionally, control samples displayed, in positive ion mode, cholesterol peaks with a much lower intensity than vitamin E signals (Fig. 3), whereas DMD-affected sections exhibited a similar or higher intensity for cholesterol signal than for vitamin E (data not shown). This is also consistent with previous findings on dystrophic muscles (51,52,53). Cholesterol, PCs and SMs colocalization, associated with a much higher proportion of cholesterol, might, therefore, suggest a tentative regulation and/or regeneration behavior of these highly damaged regions in the human DMD-affected muscles.

Fatty acyl chains composition changes

ToF-SIMS analyses of the *mdx* mouse muscle (5) revealed a calculated C18:0/C18:1 ratio value 6 to 7 times higher in the regenerating area than in the degenerating and control ones. In human samples, this ratio was only 1.5 times higher in the control spots than in the dystrophic ones (0.77 and 0.54, respectively). Besides, in studies on mouse lipid fractions, a C18:2/C18:1 ratio value of 1.3 has been reported for both healthy and predominantly nondestructured dystrophic myofilaments (52). As mentioned earlier, this is most probably due to the

significantly low amount of destructured fibers, adipose and connective tissues in the dystrophic mouse muscle (1). Similarly, a lower incorporation of C18:2 in phosphatidylcholines has been observed in human dystrophic muscles, compared to healthy ones, together with an increased level of C18:1 and C18:0 (21,22). The variation of fatty acid composition between the different areas revealed by the present study can be interpreted as an attempt to stabilize the dystrophic cells, since incorporation of saturated fatty acids in cell wall phospholipids reduces membrane flexibility. By contrast to the cells, the more damaged zones of the DMD tissues showed an increased relative abundance of monounsaturated fatty acids (C18:1) as deduced from lower R_2 and higher R_3 ratio values. Concerning the arachidonic acid carboxylate ions (C20:4), the distribution was found maximal in the degenerating zone. This fatty acid is, among others, a prostaglandin precursor that can accumulate in dystrophin deficient muscles during inflammation.

Phosphatidylinositols

The reduced relative abundance of the PI36:2 and PI36:1 compounds (*m/z* 861.6 and 863.6, respectively), with regards to the control tissue (Fig. 7C), might already hint at an increase of phospholipase activity in the DMD-affected muscle cells. PIs cycle rate is known to be reduced in dystrophic muscle cells, inducing a high local phospholipases A_2, C and D activity (54,55). As mentioned above, the decrease of PIs is accompanied by an increase of triglycerides and sphingomyelin, supporting the hypothesis of the enhanced phospholipase C activity. This increased activity is thought to be induced by the high concentration of intracellular calcium.

Conclusion

In summary, cluster-ToF-SIMS imaging allowed us to directly and relatively rapidly probe intact biological tissue sections with a complete preservation of the sample molecular and

structural integrity, a simultaneous analysis of different morphological regions at a micrometer scale and a high molecular specificity and sensitivity without any prior preparation procedure. The specific localization of the different compounds in the positive ion mode imaging and its confirmation in the negative ion mode demonstrated the absence of any molecular delocalization at the micrometer scale on the samples. Moreover, the association of the mass spectra with images was highly useful, providing, on the one hand, molecular composition even when the image contrast was low and, on the other hand, the spatial localization even with a low signal-to-noise ratio. ToF-SIMS imaging thus gives a considerable amount of information on the local molecular composition within tissues or organs, and can be recognized as a powerful approach for localized lipidomics studies. The method emerges as a promising and highly valuable indicator of the disturbance of regulation processes, like alteration of phospholipid incorporation or lipases dysfunctioning, paving the way for substantial assistance in drug-design studies or specific inhibitors development.

Acknowledgements

We thank the French *"Banque de Tissus pour la Recherche"* (*BTR, Institut de Myologie*) for providing surgery residues of human paravertebral striated muscles. The *BTR* is a partner of the EuroBioBank network funded by the EC under the Fifth Framework Programme (QLRI-CT-2002-02769). NT is indebted to the Institut de Chimie des Substances Naturelles (CNRS) for a post-doctoral grant. This work was supported by the European Union (contract LSHG-CT-2005-518194 COMPUTIS).

References

1. Blake, D.J., A. Weir, S.E. Newey, and K.E. Davies. 2002. Function and genetics of dystrophin and dystrophin-related proteins in muscle. Physiol. Rev. 82: 291-329.

2. Voisin, V., C. Sebrie, S. Matecki, H. Yu, B. Gillet, M. Ramonatxo, M. Israel, and S. De La Porte. 2005. L-arginine improves dystrophic phenotype in *mdx* mice. *Neurobiol. Dis.* **20**: 123-130.

3. Bulfield, G., W. G. Siller, P. A. Wight, and K. J. Moore. 1984. X chromosome-linked muscular dystrophy (mdx) in the mouse. *Proc. Natl. Acad. Sci. U S A.* **81**: 1189-1192.

4. Touboul, D., H. Piednoel, V. Voisin, S. De La Porte, A. Brunelle, F. Halgand, and O. Laprévote. 2004. Changes of phospholipid composition within the dystrophic muscle by matrix-assisted laser desorption/ionization mass spectrometry and mass spectrometry imaging. *Eur. J. Mass Spectrom.* **10**: 657-664.

5. Touboul, D., A. Brunelle, F. Halgand, S. De La Porte, and O. Laprevote. 2005. Lipid imaging by gold cluster time-of-flight secondary ion mass spectrometry: application to Duchenne muscular dystrophy. *J. Lipid Res.* **46**: 1388-1395.

6. Brunelle, A., D. Touboul, and O. Laprévote. 2005. Biological tissue imaging with time-of-flight secondary ion mass spectrometry and cluster ion sources. *J. Mass Spectrom.* **40**: 985-999.

7. Touboul, D., F. Kollmer, E. Niehuis, A. Brunelle, and O. Laprévote. 2005. Improvement of Biological Time-of-Flight-Secondary Ion Mass Spectrometry Imaging with a Bismuth Cluster Ion Source. *J. Am. Soc. Mass Spectrom.* **16**: 1608-1618.

8. Nygren, H., C. Eriksson, P. Malmberg, H. Sahlin, L. Carlsson, J. Lausmaa, and P. Sjövall. 2003. A cell preparation method allowing subcellular localization of cholesterol and phosphocholine with imaging TOF-SIMS. *Colloid Surf. B* **30**: 87-92.

9. Ostrowski, S. G., C. T. Van Bell, N. Winograd, and A. G. Ewing. 2004. Mass Spectrometric Imaging of Highly Curved Membranes During *Tetrahymena* Mating. *Science* **305**: 71-73.

10. Touboul, D., F. Halgand, A. Brunelle, R. Kersting, E. Tallarek, B. Hagenhoff, and O. Laprévote. 2004. Tissue molecular ion imaging by gold cluster ion bombardment. *Anal. Chem.* **76**: 1550-1559.

11. Sjövall, P., J. Lausmaa, and B. Johansson. 2004. Mass spectrometric imaging of lipids in brain tissue. Anal. Chem. 76: 4271-4278.

12. Monroe, E. B., J. C. Jurchen, J. Lee, S. S. Rubakhin, and J. V. Sweedler. 2005. Vitamin E imaging and localization in the neuronal membrane. J. Am. Chem. Soc. 127: 12152-12153.

13. Nygren, H., K. Börner, P. Malmberg, E. Tallarek, and B. Hagenhoff. 2005. Imaging TOF-SIMS of rat kidney prepared by high-pressure freezing. *Microsc. Res. Tech.* **68**: 329-334.

14. Nygren, H., K. Börner, P. Malmberg, and B. Hagenhoff. 2006. Localization of cholesterol in rat cerebellum with imaging TOF-SIMS - Effect of tissue preparation. *Appl. Surf. Sci.* **252**: 6975-6981.

15. Mas, S., D. Touboul, A. Brunelle, P. Aragoncillo, J. Egido, O. Laprévote, and F. Vivanco. 2007. Lipid cartography of atherosclerotic plaque by cluster-TOF-SIMS imaging. *Analyst.* **132**: 24-26.

16. Touboul, D., S. Roy, D. P. Germain, P. Chaminade, A. Brunelle, and O. Laprévote. 2007. MALDI-TOF and cluster-TOF-SIMS imaging of Fabry disease biomarkers. *Int. J. Mass Spectrom.* **260**: 158-165.

17. Veryovkin, I.V., S.F. Belykh, A. Adriaens, A.V. Zinovev, and F. Adams. 2004. On the trends in kinetic energies of secondary ions produced by polyatomic ion bombardment. *App. Surf. Sci.* **231-232**: 101-105.

18. Gilmore, I. S., and M. P. Seah. 2000. Ion detection efficiency in SIMS: dependencies on energy, mass and composition for microchannel plates used in mass spectrometry. *Int. J. Mass Spectrom.* **202**: 217-229.

19. Touboul, D., A. Brunelle, and O. Laprévote. 2006. Structural analysis of secondary ions by post-source decay in time-of-flight secondary ion mass spectrometry. *Rapid Commun. Mass Spectrom.* **20**: 703-709.

20. Börner, K., H. Nygren, B. Hagenhoff, P. Malmberg, E. Tallarek, and J.E. Månsson. 2006. Distribution of cholesterol and galactosylceramide in rat cerebellar white matter. *Biochim. Biophys. Acta* **1761**: 335-344.

21. Pearce, P. H., R. D. Johnsen, S. J. Wysocki, and B. A. Kakulas. 1981. Muscle lipids in Duchenne muscular dystrophy. *Aust. J. Exp. Biol. Med.* **59**: 77-90.

22. Kunze, D., G. Reichmann, E. Egger, D. Olthoff, and K. Dohler. 1975. Fatty acid pattern of lipids in normal and dystrophic human muscle. *Eur. J. Clin. Invest.* **5**: 471-475.

23. Wiseman, J. M., S. M. Puolitaival, Z. Takats, R. G. Cooks, and R. M. Caprioli. 2005. Mass spectrometric profiling of intact biological tissue by using desorption electrospray ionization. *Angew. Chem. Int. Ed.* **44**: 7094-7097.

24. Zhang, Y. H., M. R. Vasko, and G. D. Nicol. 2002. Ceramide, a putative second messenger for nerve growth factor, modulates the TTX-resistant Na(+) current and delayed rectifier K(+) current in rat sensory neurons. *J. Physiol.* **544**: 385-402.

25. Titievsky, A., I. Titievskaya, M. Pasternack, K. Kaila, and K. Tornquist. 1998. Sphingosine inhibits voltage-operated calcium channels in GH4C1 cells. *J. Biol. Chem.* **273**: 242-247.

26. Nygren, H., K. Börner, B. Hagenhoff, P. Malmberg, and J. E. Månsson. 2005. Localization of cholesterol, phosphocholine and galactosylceramide in rat cerebellar cortex with imaging TOF-SIMS equipped with a bismuth cluster ion source. *Biochim. Biophys. Acta.* **1737**: 102-110.

27. Slotte, J. P. 1997. Cholesterol-sphingomyelin interactions in cells--effects on lipid metabolism. *Subcell. Biochem.* **28**: 277-293.

28. Ohvo-Rekila, H., B. Ramstedt, P. Leppimaki, and J. P. Slotte. 2002. Cholesterol interactions with phospholipids in membranes. *Prog. Lipid Res.* **41**: 66-97.

29. Ramstedt, B., and J. P. Slotte. 2002. Membrane properties of sphingomyelins. *FEBS Lett.* **531**: 33-37.

30. Hsu, F. F., and J. Turk. 2000. Characterization of phosphatidylinositol, phosphatidylinositol-4-phosphate, and phosphatidylinositol-4,5-bisphosphate by electrospray ionization tandem mass spectrometry: a mechanistic study. *J. Am. Soc. Mass Spectrom.* **11**: 986-999.

31. Stroobant, V., R. Rozenberg, E. M. Bouabsa, E. Deffense, and E. de Hoffmann. 1995. Fragmentation of conjugate bases of esters derived from multifunctional alcohols including triacylglycerols. *J. Am. Soc. Mass. Spectrom.* **6**: 498-506.

32. Li, C., and J. A. Yergey. 1997. Continuous flow liquid secondary ion mass spectrometric characterization of phospholipid molecular species. *J. Mass Spectrom.* **32**: 314-322.

33. Murphy, R. C. 1993. Mass Spectrometry of Lipids (Handbook of Lipid Research, Vol. 7). Plenum Press, New York.

34. Ostrowski, S. G., C. Szakal, J. Kozole, T. P. Roddy, J. Xu, A. G. Ewing, and N. Winograd. 2005. Secondary ion MS imaging of lipids in picoliter vials with a buckminsterfullerene ion source. *Anal Chem.* **77**: 6190-6196.

35 Wenk M.R., L. Lucast, G. Di Paolo, A.J. Romanelli, S.F. Suchy, R.L. Nussbaum, G.W. Cline, G.I. Shulman, W. McMurray, and P. De Camilli. 2003. Phosphoinositide profiling in complex lipid mixtures using electrospray ionization mass spectrometry. *Nat. Biotechnol.***21**: 813-817.

36. Bonsett, C. A., and A. Rudman. 1994. 'Oil globules' in Duchenne muscular dystrophy--history, demonstration, and metabolic significance. *Med. Hypotheses.* **43**: 327-338.

37. Fahy, E., S. Subramaniam, H. A. Brown, C. K. Glass, A. H. Merrill, Jr., R. C. Murphy, C. R. Raetz, D. W. Russell, Y. Seyama, W. Shaw, T. Shimizu, F. Spener, G. van Meer, M. S. van Nieuwenhze, S. H. White, J. L. Witztum, and E. A. Dennis. 2005. A comprehensive classification system for lipids. *J. Lipid Res.* **46**: 839-861.

38. Simons, K., and E. Ikonen. 2000. How cells handle cholesterol. *Science.* **290**: 1721-1726.

39. Simons, K., and E. Ikonen. 1997. Functional rafts in cell membranes. *Nature.* **387**: 569-572.

40. Pfrieger, F. W. 2003. Role of cholesterol in synapse formation and function. *Biochim. Biophys. Acta.* **1610**: 271-280.

41. Sjövall, P., J. Lausmaa, H. Nygren, L. Carlsson, and P. Malmberg. 2003. Imaging of membrane lipids in single cells by imprint-imaging time-of-flight secondary ion mass spectrometry. *Anal. Chem.* **75**: 3429-3434.

42. Touboul D., S. Roy, D.P. Germain, P. Chaminade, A. Brunelle, and O. Laprévote. 2007. MALDI-TOF and cluster-TOF-SIMS imaging of Fabry disease biomarkers. *Int. J. Mass Spectrom.* **260**: 158-165.

43. Kolesnick, R. N., and M. Kronke. 1998. Regulation of ceramide production and apoptosis. *Annu. Rev. Physiol.* **60**: 643-665.

44. Kim, C. W., H. M. Lee, T. H. Lee, C. Kang, H. K. Kleinman, and Y. S. Gho. 2002. Extracellular membrane vesicles from tumor cells promote angiogenesis via sphingomyelin. *Cancer Res.* **62**: 6312-6317.

45. Kwok, C. T., and L. Austin. 1978. Phospholipid composition and metabolism in mouse muscular dystrophy. *Biochem. J.* **176**: 15-22.

46. Banerjee, A. K., and S. Goyle. 1983. Altered lipid composition of adipose tissue in human muscular dystrophy. *Biochem. Med.* **30**: 246-252.

47. Ullman, M. D., and N. S. Radin. 1974. The enzymatic formation of sphingomyelin from ceramide and lecithin in mouse liver. *J. Biol. Chem.* **249**: 1506-1512.

48. Kanfer, J. N., and C. H. Spielvogel. 1975. Phospholipase C catalyzed formation of sphinogomyelin--14C from lecithin and N-(-14C)-oleoyl-sphingosine. Lipids. **10**: 391-394.

49. Schiller, J., J. Arnhold, H. J. Glander, and K. Arnold. 2000. Lipid analysis of human spermatozoa and seminal plasma by MALDI-TOF mass spectrometry and NMR spectroscopy - effects of freezing and thawing. *Chem. Phys. Lipids.* **106**: 145-156.

50. Schiller, J., O. Zschornig, M. Petkovic, M. Muller, J. Arnhold, and K. Arnold. 2001. Lipid analysis of human HDL and LDL by MALDI-TOF mass spectrometry and (31)P-NMR. *J Lipid Res.* **42**: 1501-1508.

51. Young, H. L., W. Young, and I. S. Edelman. 1959. Electrolyte and lipid composition of skeletal and cardiac muscle in mice with hereditary muscular dystrophy. *Am. J. Physiol.* **197**: 487-490.

52. Owens, K., and B. P. Hughes. 1970. Lipids of dystrophic and normal mouse muscle: whole tissue and particulate fractions. *J. Lipid Res.* **11**: 486-495.

53. Logan, D. M., and K. H. Tsang. 1992. Cholesterol alterations in young dystrophic mice. *Mol. Cell Biochem.* **110**: 55-64.

54. Rounds, P. S., A. B. Jepson, D. J. McAllister, and J. L. Howland. 1980. Stimulated turnover of phosphatidylinositol and phosphatidate in normal and Duchenne-dystrophic human skin fibroblasts. *Biochem. Biophys. Res. Commun.* **97**: 1384-1390.

55. Liberona, J. L., J. A. Powell, S. Shenoi, L. Petherbridge, R. Caviedes, and E. Jaimovich. 1998. Differences in both inositol 1,4,5-trisphosphate mass and inositol 1,4,5-trisphosphate receptors between normal and dystrophic skeletal muscle cell lines. *Muscle Nerve.* **21**: 902-909.

Figure captions:

Figure 1:

Microscope images of 20 µm thick sections of human striated muscle surgery residues before ToF-SIMS analyses. Some of the analyzed spots are delimited by the green squares. The scale has been added at the bottom of each image.

A) Control section.

B) DMD-affected section.

Figure 2:

Trichrome Masson histological staining of 10 µm thick muscle sections. Red: cytoplasm, blue: collagen).

A) Control section.

B) DMD-affected section.

Figure 3:

ToF-SIMS total mass spectrum of spot 1 (control, see Fig. 1A) in positive ion mode.

Figure 4:

ToF-SIMS analysis of spot 1 (control, see Fig. 1A) in positive ion mode.

A) From left to right: microscope image; *m/z* 758 and *m/z* 760 ions images with maximal number of counts in a pixel (*mc*) for the color scale and image total number of counts (*tc*), field of view 500x500 μm^2, compressed to 128x128 pixels, averaged and rescaled; selected ROIs (red, green, blue = cells, pink = intercellular space).

B) *m/z* [650-820] enlargement of each ROI's spectrum.

C) R_1 (758/760) ratio for each selected ROI.

Figure 5:

ToF-SIMS analysis of spot 2 (DMD, see Fig. 1B) in positive ion mode.

A) From left to right: microscope image; *m/z* 758 and *m/z* 760 ion images with maximal number of counts in a pixel (*mc*) for the color scale and image total number of counts (*tc*), field of view 500x500 μm^2, compressed to 128x128 pixels, averaged and rescaled; selected ROIs (red, green, blue = cells, yellow = intercellular space).

B) *m/z* [650-820] enlargement of each ROI's spectrum.

C) R_1 (758/760) ratio for each selected ROI.

Figure 6:

ToF-SIMS analysis of spot 3 (DMD, see Fig. 1B) in positive ion mode.

A) From left to right: microscope image; *m/z* 758 and *m/z* 760 ion images with maximal number of counts in a pixel (*mc*) for the color scale and image total number of counts (*tc*), field of view 500x500 μm^2, compressed to 128x128 pixels, averaged and rescaled; selected ROIs (red = cells, green = damaged area, blue = adipocytes).

B) *m/z* [650-820] enlargement of each ROI's spectrum.

C) R_1 (758/760) ratio for each selected ROI.

Figure 7:

ToF-SIMS global spectra of control and DMD-affected striated human muscle sections.

A) Positive ion mode: *m/z* [650-820] mass range (phosphatidylcholines and sphingomyelins).

B) Negative ion mode: *m/z* [240-320] (fatty acid carboxylate ions).

C) Negative ion mode: *m/z* [760-920] (phosphatidylinositols and triglycerides).

Figure 8:

ToF-SIMS ion images of spot 3 (see Fig. 1B). Below each ion image: name of the selected species, with maximal number of counts in a pixel (*mc*) for the color scale and image total number of counts (*tc*). Some images are the result of the sum of several ion images, after verification of their exact colocalization.

A) Negative ion mode. From left to right: sum of the SM fragment ion (*m/z* 616, 642 and 687); cholesterol; cholesteryl sulfate; vitamin E deprotonated molecule.

B) Positive ion mode. First line from left to right: microscope image; choline fragment (*m/z* 86), protonated choline molecule (*m/z* 104 ion image); PC headgroup (*m/z* 184 ion image). Second line from left to right: PC fragments (sum of *m/z* 125, 166, 206, 224 and 246 ion images); *m/z* 758 and *m/z* 760 ion images. Third line: SM fragment (*m/z* 668); sum of SM protonated and sodiated species (*m/z* 703 and 725); vitamin E molecular ion.

Figure 9:

ToF-SIMS analysis of spot 3 (see Fig. 1B) in negative ion mode.

A) Mass spectra (*m/z* [760-920]) of each of the selected ROI's.

B) Ion images of the corresponding detected ions, with the mass range and class of affiliation (number of unsaturations) of the selected species, with maximal number of counts in a pixel (*mc*) for the color scale and image total number of counts (*tc*).

Table I: R_1 ratios calculated for each control and dystrophic spot. $R_1 = I_{m/z\ 758} / I_{m/z\ 760}$: ratio of the intensity of the PC34:2 protonated molecule signal at *m/z* 758.6 over the corrected intensity of the PC34:1 protonated molecule signal at *m/z* 760.6. Data originate from positive ion mode ToF-SIMS analyses on four human striated muscle sections from a control and on two sections from two distinct DMD-affected children. The spots correspond to areas over which ToF-SIMS imaging mass spectrometry experiments were carried out.

Sample	Section number	Spot number	Spot Ratio R_1	Section average value	Standard deviation	Sample average value	Standard deviation
DMD Child 1	1	1 2 3 4	1.13 1.27 1.13 0.99	1.00	± 0.11	**1.15**	**± 0.17**
	2	1 2 3 4 5 6	0.84 1.04 0.90 1.14 1.08 1.02	1.13	± 0.11		
DMD Child 2	3	1 2 3 4 5	1.54 1.42 1.07 1.37 1.20	1.32	± 0.19		
	4	1 2 3 4 5	1.25 1.23 0.94 1.18 1.19	1.16	± 0.13		
Control	1	1 2 3 4 5	1.89 1.82 1.73 2.22 2.16	1.96	± 0.22	**1.85**	**± 0.31**
	2	1 2	2.06 2.28	2.17	± 0.16		
	3	1 2 3	1.79 1.89 1.22	1.63	± 0.36		
	4	1 2 3	1.99 1.50 1.47	1.65	± 0.29		

Table II: R_2 ratios calculated for each control and dystrophic spot. $R_2 = I_{m/z\ 283} / I_{m/z\ 281}$: ratio of the corrected intensity of the C18:0 fatty acid carboxylate signal at *m/z* 283.2 over the intensity of the C18:1 fatty acid carboxylate signal at *m/z* 281.2. Data originate from negative ion mode ToF-SIMS analyses on four human striated muscle sections from a control and on two sections from two distinct DMD-affected children. The spots correspond to areas over which ToF-SIMS imaging mass spectrometry experiments were carried out.

Sample	**Section number**	**Spot number**[a]	**Spot Ratio R_2**[b]	**Section average value**	**Standard deviation**	**Sample average value**	**Standard deviation**
DMD Child 1	1	1 2 3 4	0.41 0.66 0.30 0.29	0.42	± 0.17	**0.54**	**± 0.14**
	2	1 2 3 4 5 6	0.44 0.73 0.58 0.66 0.54 0.76	0.62	± 0.12		
DMD Child 2	3	1 2 3 4 5	0.70 0.42 0.45 0.57 0.35	0.50	± 0.14		
	4	1 2 3 4 5	0.73 0.52 0.50 0.52 0.60	0.59	± 0.09		
Control	1	1 2 3 4 5	1.09 0.65 0.75 0.77 0.50	0.75	± 0.12	**0.77**	**± 0.16**
	2	1 2	0.63 0.63	0.63	± 0.00		
	3	1 2 3	0.88 0.92 0.84	0.88	± 0.04		
	4	1 2 3	0.72 0.91 0.69	0.77	± 0.12		

Table III: R_3 ratios calculated for each control and dystrophic spot. $R_3 = I_{m/z\ 281} / I_{m/z\ 279}$: ratio of the corrected intensity of the C18:1 fatty acid carboxylate signal at *m/z* 281.2 over the intensity of the C18:2 fatty acid carboxylate signal at *m/z* 279.2. Data originate from negative ion mode ToF-SIMS analyses on four human striated muscle sections from a control and on two sections from two distinct DMD-affected children. The spots correspond to areas over which ToF-SIMS imaging mass spectrometry experiments were carried out.

Sample	Section number	Spot number	Spot Ratio R_3	Section average value	Standard deviation	Sample average value	Standard deviation
DMD Child 1	1	1 2 3 4	2.67 1.74 2.41 2.33	2.29	± 0.39	**1.96**	**± 0.45**
	2	1 2 3 4 5 6	2.74 1.86 2.46 1.77 2.03 1.52	2.06	± 0.46		
DMD Child 2	3	1 2 3 4 5	1.09 1.62 2.15 1.71 2.22	1.76	± 0.46		
	4	1 2 3 4 5	1.20 1.93 2.25 1.50 2.08	1.79	± 0.43		
Control	1	1 2 3 4 5	0.74 1.18 1.03 0.88 1.14	0.99	± 0.18	**0.98**	**± 0.18**
	2	1 2	1.00 0.85	0.93	± 0.11		
	3	1 2 3	0.78 0.81 1.30	0.96	± 0.29		
	4	1 2 3	0.92 0.90 1.21	1.01	± 0.17		

A: CONTROL section

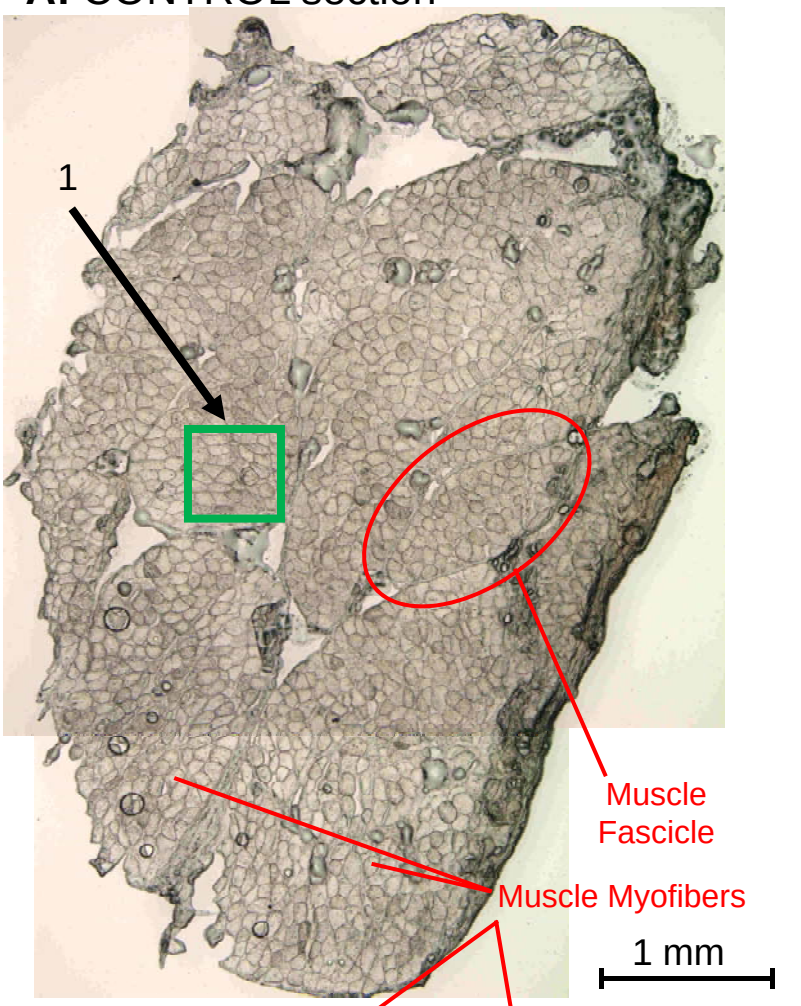

B: DMD section

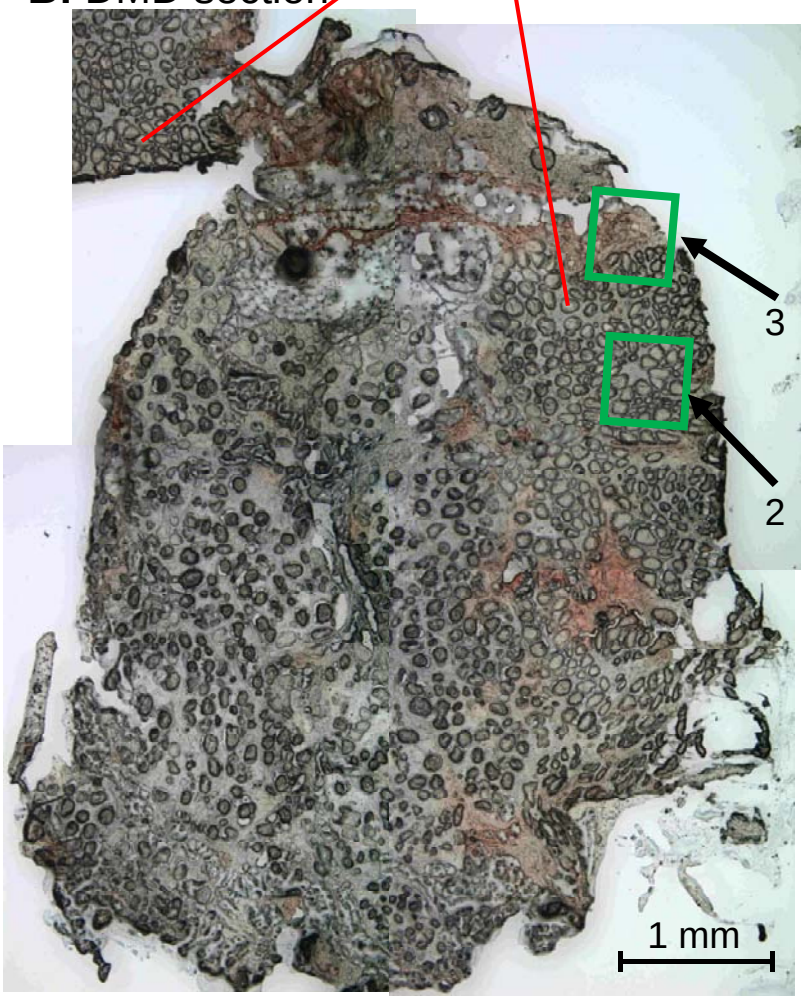

Figure 1

A: CONTROL section

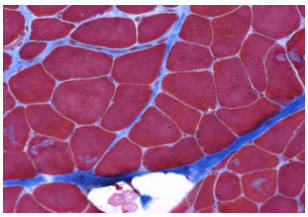

Magnification 20

109 µm

B: DMD section

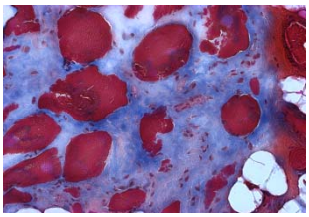

Magnification 20

109 µm

Figure 2

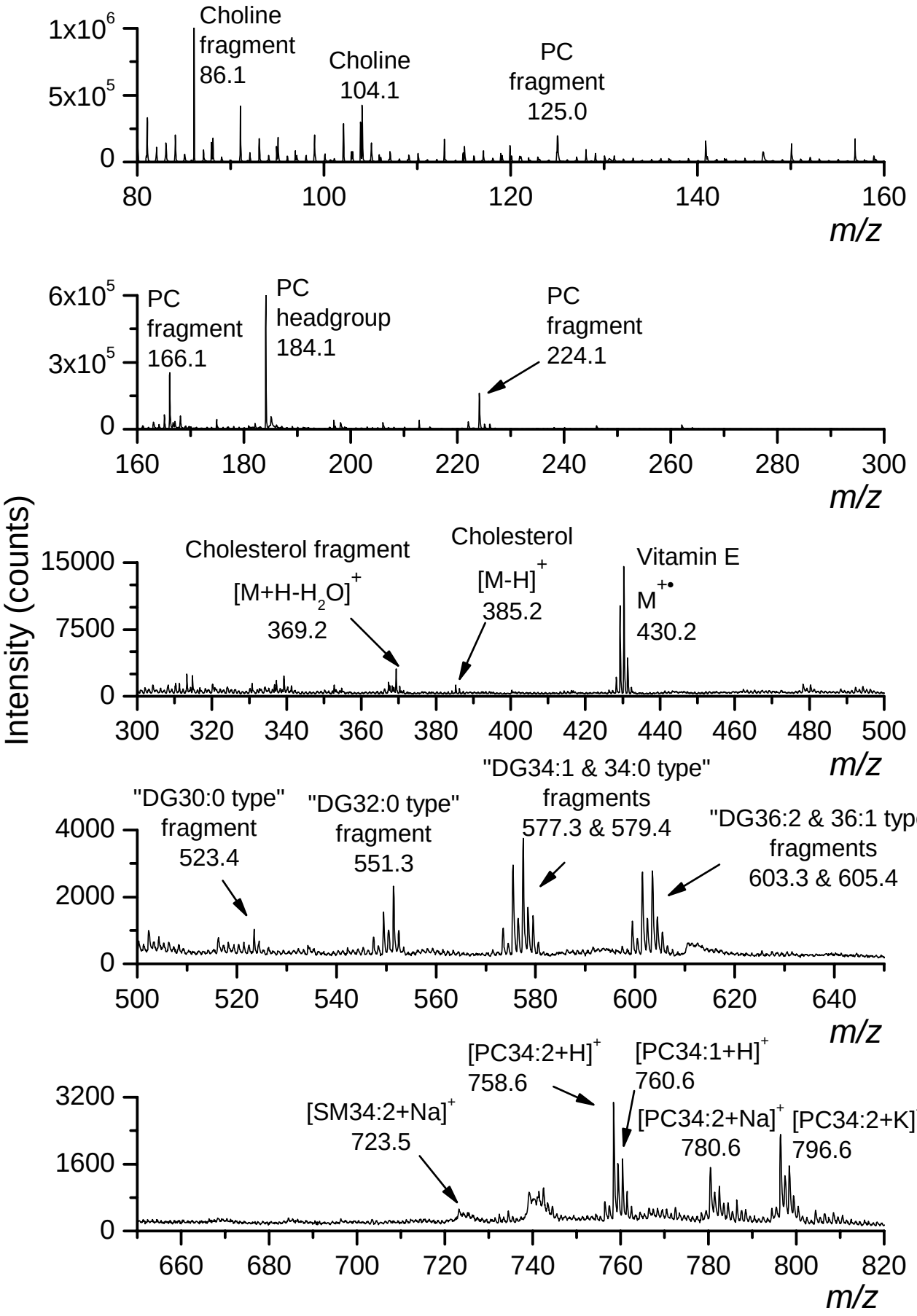
Intensity (counts)
1x10^6
5x10^5
0
Choline fragment 86.1
Choline 104.1
PC fragment 125.0
80
100
120
140
160
m/z
6x10^5
3x10^5
0
PC fragment 166.1
PC headgroup 184.1
PC fragment 224.1
160
180
200
220
240
260
280
300
m/z
15000
7500
0
Cholesterol fragment
[M+H-H2O]+
369.2
Cholesterol
[M-H]+
385.2
Vitamin E
M+•
430.2
300
320
340
360
380
400
420
440
460
480
500
m/z
4000
2000
0
"DG30:0 type" fragment 523.4
"DG32:0 type" fragment 551.3
"DG34:1 & 34:0 type" fragments 577.3 & 579.4
"DG36:2 & 36:1 type" fragments 603.3 & 605.4
500
520
540
560
580
600
620
640
m/z
3200
1600
0
[PC34:2+H]+
758.6
[PC34:1+H]+
760.6
[SM34:2+Na]+
723.5
[PC34:2+Na]+
780.6
[PC34:2+K]+
796.6
660
680
700
720
740
760
780
800
820
m/z

Figure 3

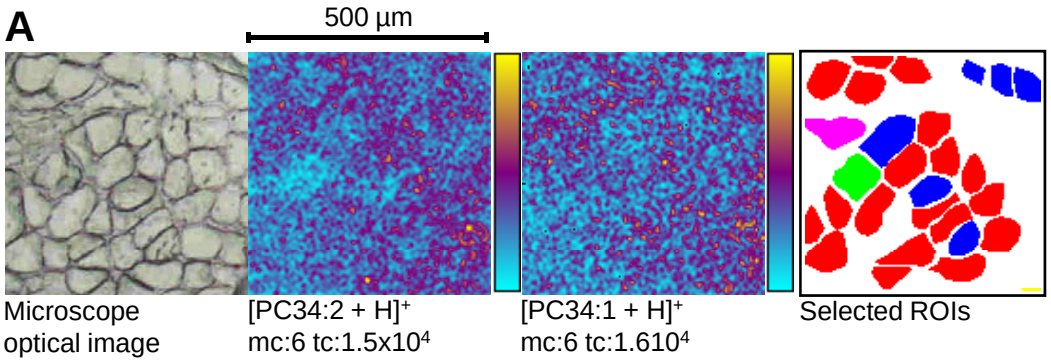
A
500 µm
Microscope
optical image
[PC34:2 + H]+
mc:6 tc:1.5x10^4
[PC34:1 + H]+
mc:6 tc:1.610^4
Selected ROIs

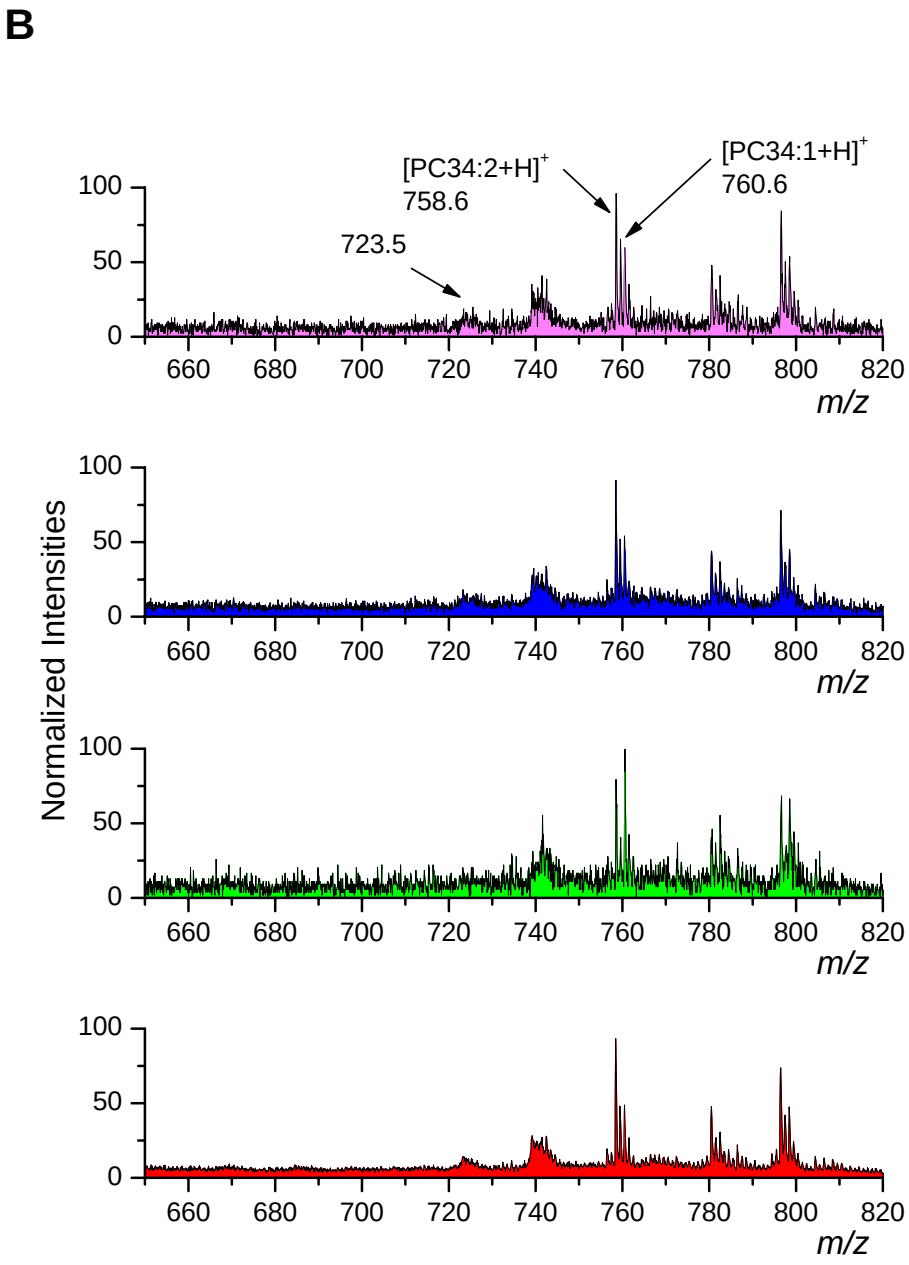
B
[PC34:2+H]+
758.6
[PC34:1+H]+
760.6
723.5
Normalized Intensities
m/z

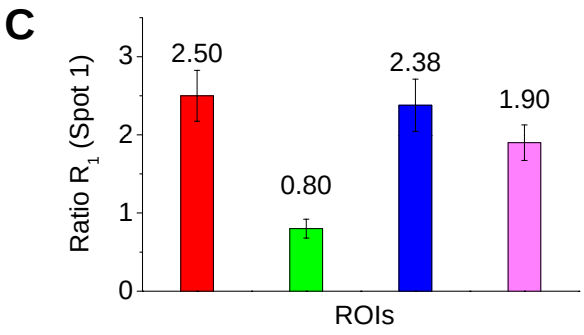
C
Ratio R1 (Spot 1)
2.50
0.80
2.38
1.90
ROIs

Figure 4

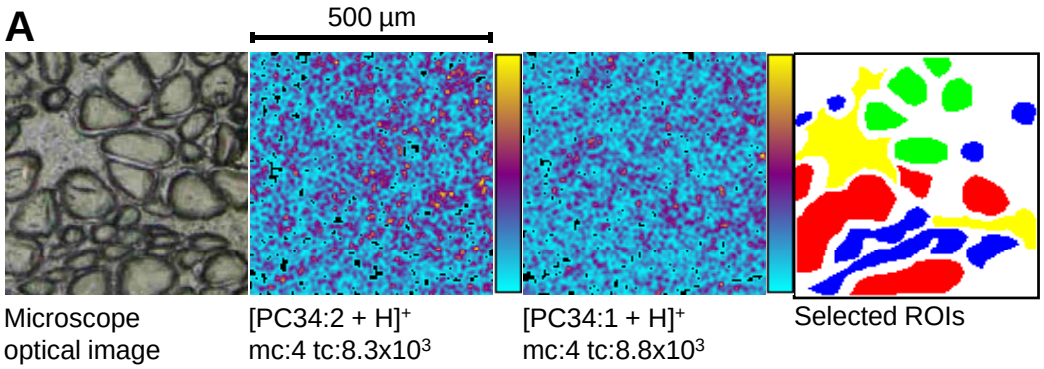
A
500 µm
Microscope optical image
[PC34:2 + H]+ mc:4 tc:8.3x10^3
[PC34:1 + H]+ mc:4 tc:8.8x10^3
Selected ROIs

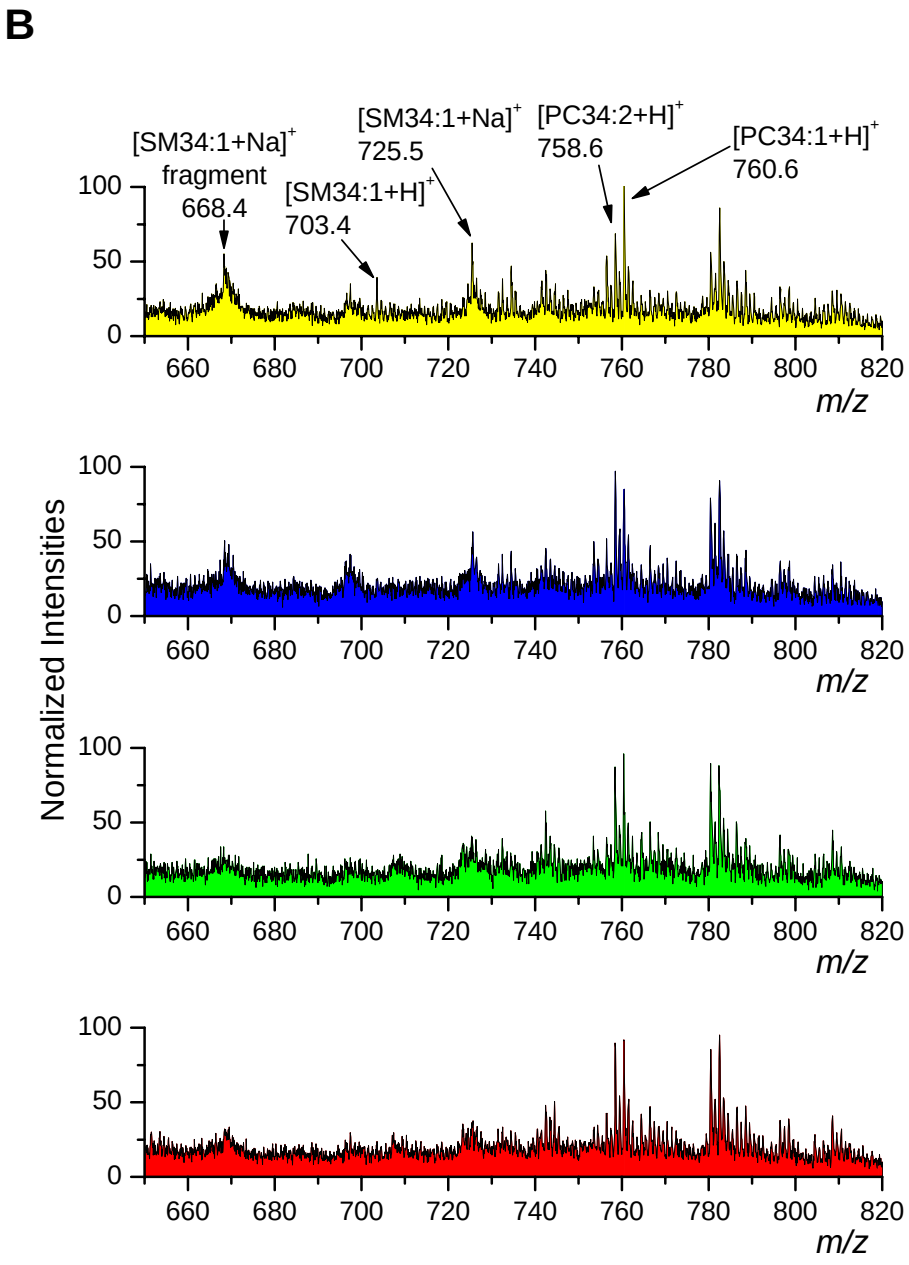
B
[SM34:1+Na]+ fragment 668.4
[SM34:1+H]+ 703.4
[SM34:1+Na]+ 725.5
[PC34:2+H]+ 758.6
[PC34:1+H]+ 760.6
Normalized Intensities
m/z

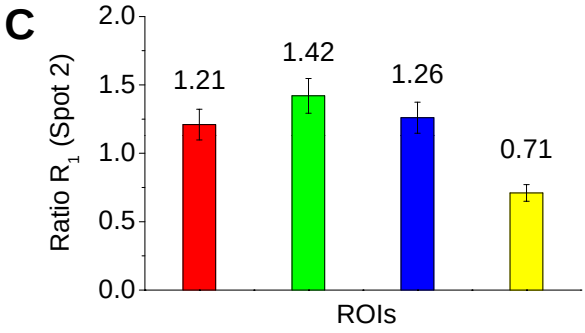
C
Ratio R1 (Spot 2)
1.21
1.42
1.26
0.71
ROIs

Figure 5

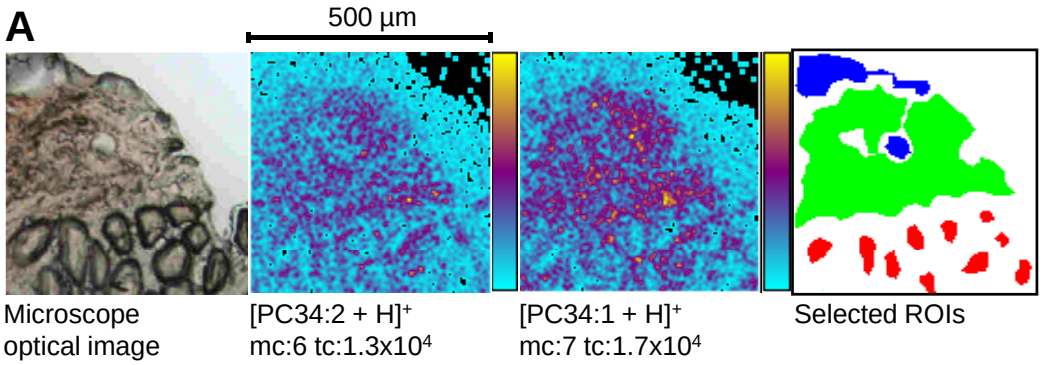
A
500 µm
Microscope optical image
[PC34:2 + H]+ mc:6 tc:1.3x10^4
[PC34:1 + H]+ mc:7 tc:1.7x10^4
Selected ROIs

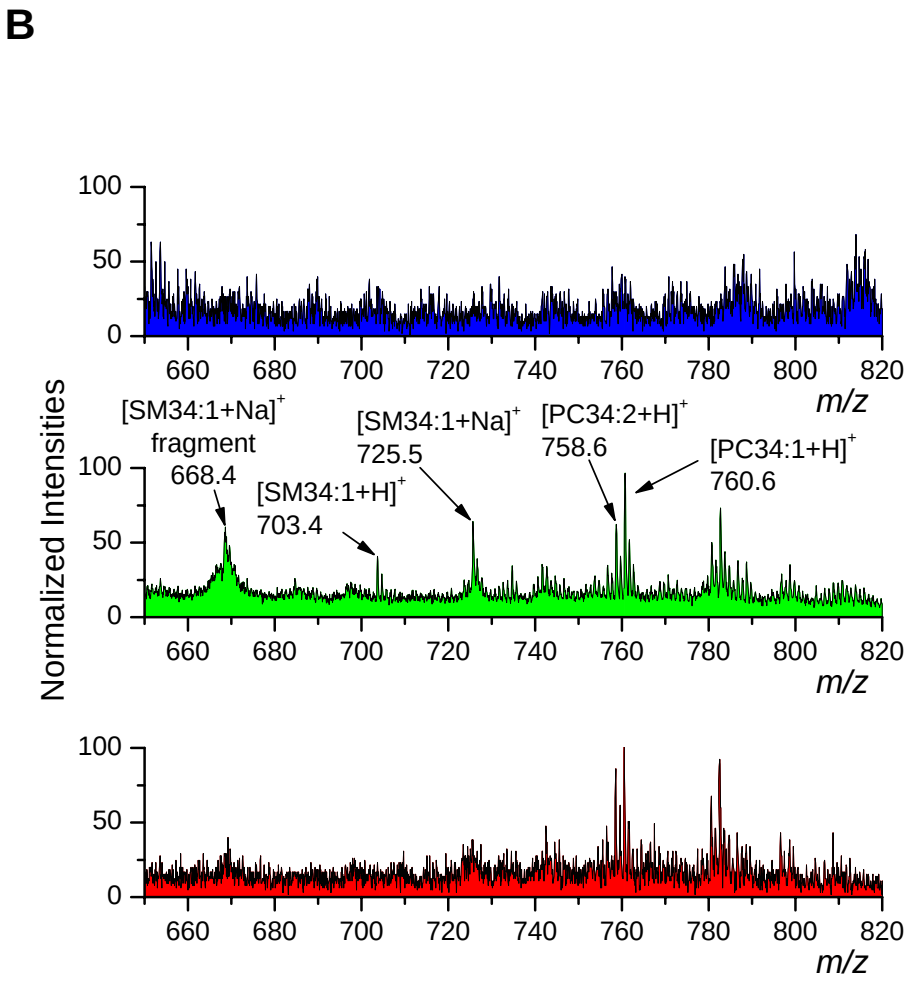
B
Normalized Intensities
[SM34:1+Na]+ fragment 668.4
[SM34:1+H]+ 703.4
[SM34:1+Na]+ 725.5
[PC34:2+H]+ 758.6
[PC34:1+H]+ 760.6
m/z

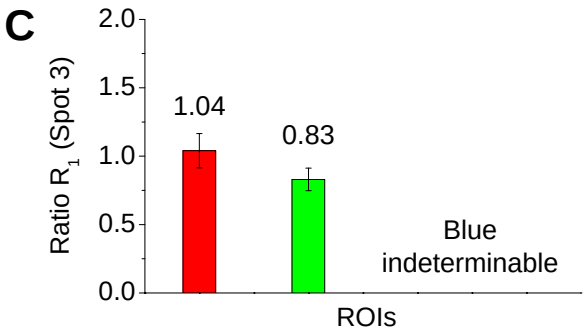
C
Ratio R1 (Spot 3)
1.04
0.83
Blue indeterminable
ROIs

Figure 6

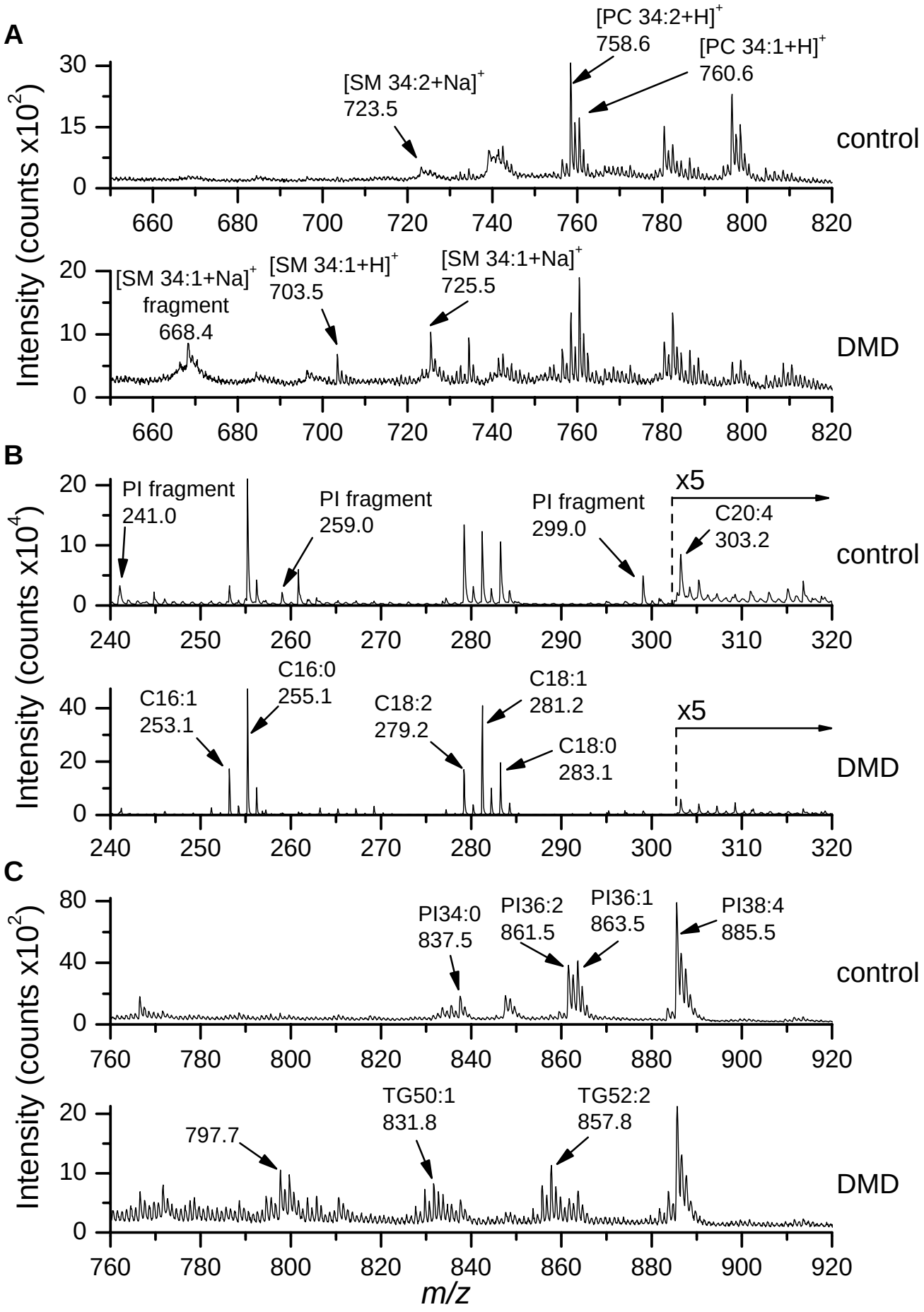
A
[PC 34:2+H]+
758.6
[PC 34:1+H]+
760.6
[SM 34:2+Na]+
723.5
control
[SM 34:1+Na]+
fragment
668.4
[SM 34:1+H]+
703.5
[SM 34:1+Na]+
725.5
DMD
Intensity (counts x10^2)
B
PI fragment
241.0
PI fragment
259.0
PI fragment
299.0
x5
C20:4
303.2
control
C16:1
253.1
C16:0
255.1
C18:2
279.2
C18:1
281.2
C18:0
283.1
x5
DMD
Intensity (counts x10^4)
C
PI34:0
837.5
PI36:2
861.5
PI36:1
863.5
PI38:4
885.5
control
797.7
TG50:1
831.8
TG52:2
857.8
DMD
Intensity (counts x10^2)
m/z

Figure 7

A Negative ion mode

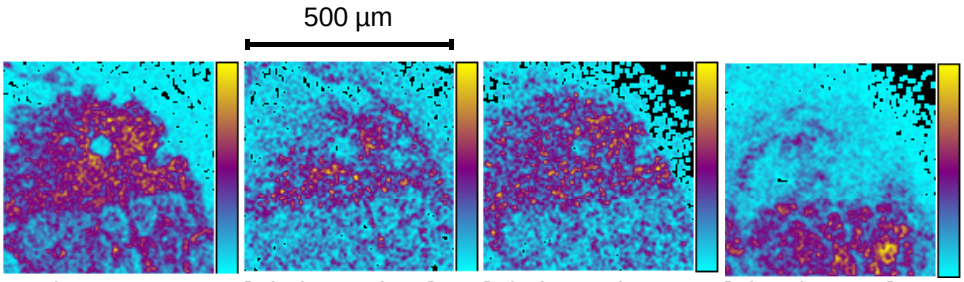

SM fragments
mc:12 tc:4.2x10^4

[Cholesterol - H]$^-$
mc:6 tc:1.5x10^4

[Cholesteryl Sulfate - H]$^-$
mc:6 tc:1.5x10^4

[Vitamin E - H]$^-$
mc:14 tc:3.5x10^5

B Positive ion mode

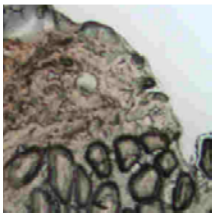

Microscope optical image

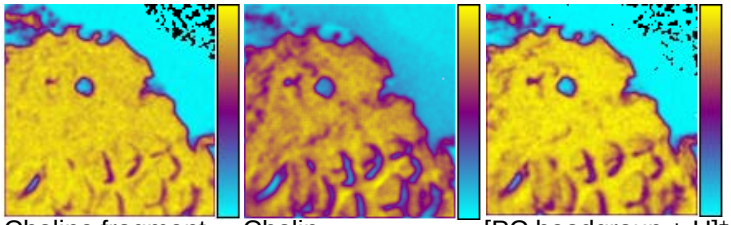

Choline fragment
mc:141 tc:1.4x10^6

Cholin
mc:197 tc:1.7x10^6

[PC headgroup + H]$^+$
mc:136 tc:1.3x10^6

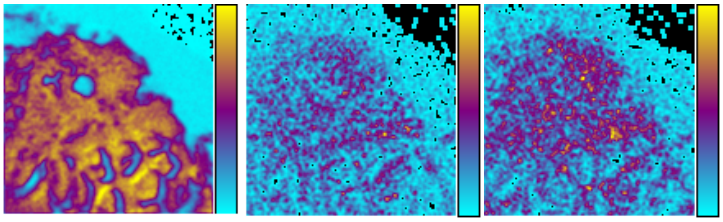

PC fragments
mc:159 tc:1.2x10^6

[PC34:2 + H]$^+$
mc:6 tc:1.3x10^4

[PC34:1 + H]$^+$
mc:7 tc:1.7x10^4

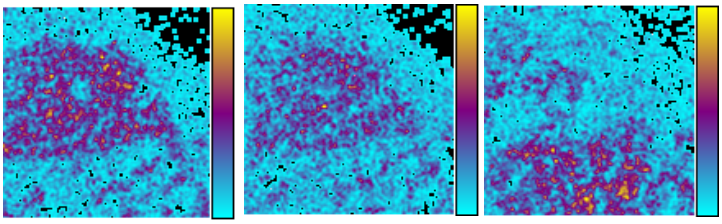

SM fragment
mc:6 tc:1.2x10^4

SM34:1 species
mc:5 tc:1.1x10^4

[Vitamin E]$^{+\bullet}$
mc:7 tc:1.3x10^4

Figure 8

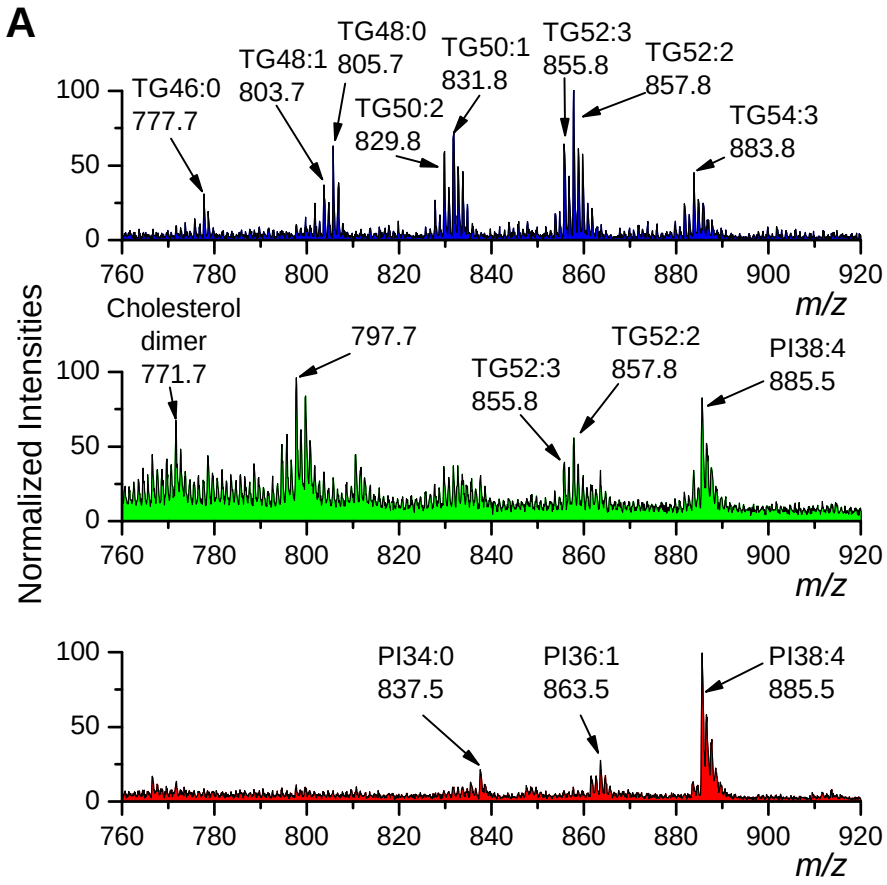
A
TG46:0
777.7
TG48:1
803.7
TG48:0
805.7
TG50:2
829.8
TG50:1
831.8
TG52:3
855.8
TG52:2
857.8
TG54:3
883.8
Normalized Intensities
m/z
Cholesterol
dimer
771.7
797.7
TG52:3
855.8
TG52:2
857.8
PI38:4
885.5
PI34:0
837.5
PI36:1
863.5
PI38:4
885.5

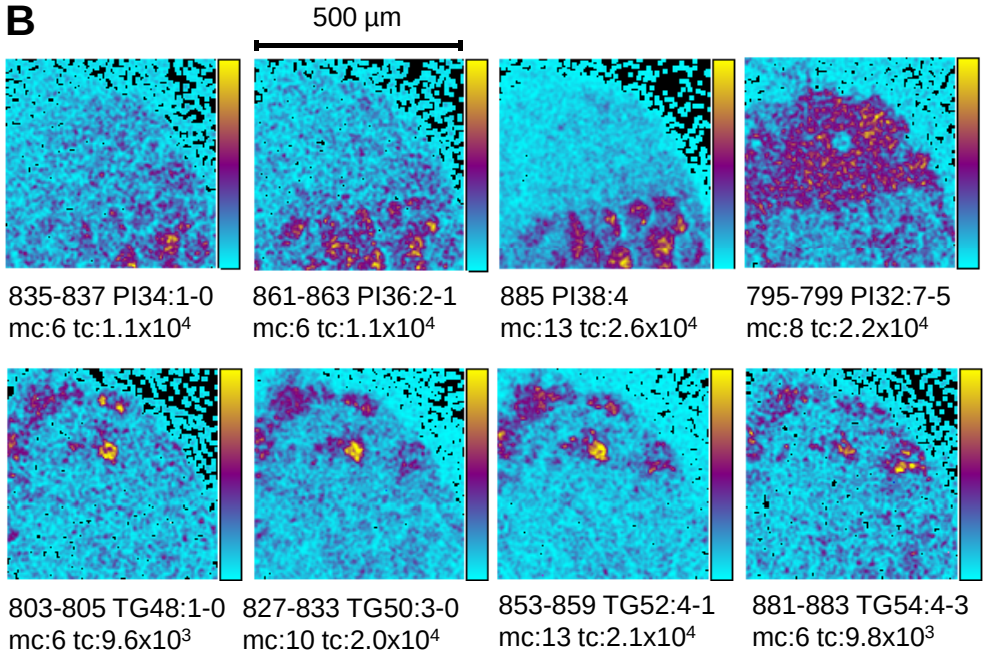
B
500 µm
835-837 PI34:1-0
mc:6 tc:1.1x10⁴
861-863 PI36:2-1
mc:6 tc:1.1x10⁴
885 PI38:4
mc:13 tc:2.6x10⁴
795-799 PI32:7-5
mc:8 tc:2.2x10⁴
803-805 TG48:1-0
mc:6 tc:9.6x10³
827-833 TG50:3-0
mc:10 tc:2.0x10⁴
853-859 TG52:4-1
mc:13 tc:2.1x10⁴
881-883 TG54:4-3
mc:6 tc:9.8x10³

Figure 9